Development of an Adaptive Discharge Coefficient to Improve the Accuracy of Cross-ventilation Airflow Calculation in Building Energy Simulation Tools

Mohammadreza Shirzadi[a], Parham A. Mirzaei[b], Mohammad Naghashzadegan[a,1]

[a] Mechanical Engineering Department, University of Guilan, Rasht, Iran
[b] Architecture and Built Environment Department, University of Nottingham, Nottingham, UK

Abstract

Airflow network (AFN) model embedded in building energy simulation (BES) tools such as EnergyPlus is extensively used for prediction of cross-ventilation in buildings. The noticeable uncertainty in the measurement of the surface pressure, discharge coefficient, and simplifications applied to the orifice-based equation result in considerable discrepancies in the prediction of the cross-ventilation airflow rate values. Computational Fluid Dynamics (CFD) provides more accurate results comparing to the orifice-based equations although with an excessive computational cost.

The aim of this study is, therefore, to improve the accuracy of the orifice-based model by development of an adaptive correlation for the discharge coefficient using CFD. Hence, a validated CFD model for the cross-ventilation of an unsheltered building is firstly developed using an experimental study. In the next step, by exploiting Latin hypercube sampling (LHS) approaches, a large CFD dataset of 750 scenarios for different building geometries (i.e. square cube, cuboid and long corridor) is generated; the dataset is then coupled to the AFN cross-ventilation model to obtain an adaptive correlation for the discharge coefficient as a function of the openings' geometries and location using response surface (RSM) and radial basis function (RBF) models.

Results show that the newly developed adaptive correlation successfully increases the accuracy of AFN model for the cross-ventilation modeling of unsheltered buildings as the relative errors for the airflow rate prediction of different building geometries are significantly decreased up to 28% in comparison with the cases with constant discharge coefficient and surface-averaged and local-surface wind pressure coefficients. Results, also demonstrate the importance of considering the value of the local-surface wind pressure in the AFN model for the square cube and cuboid building models.

Keywords: Cross-ventilation, CFD, Sampling, Discharge coefficient, Building Energy Simulation, Correlation

[1] Corresponding author: Khalij Fars highway, Rasht, Iran
Tel.: 013-33690274; Postal Code: 4199613776
Email: naghash@guilan.ac.ir

Nomenclature

ρ	Density	U_H	Inflow mean streamwise velocity at building height H
t	Time	H	Building height
x, y, z	Component of space coordinate	α	Power-law exponent
U_i	Component of mean velocity vector	N	Number of data points
S_{M_i}	Momentum source	O_i	Observed value
k	Turbulent kinetic energy	P_i	Predicted value
μ_l	Molecular viscosity	$FAC2$	Fraction of the predictions within a factor of 2 of the observations
C_μ	Turbulence model constant	$NMSE$	Normalized mean square error
ε	Turbulent dissipation rate	u_i	Fluctuating velocity component in turbulent flow
D	Building depth	C_p	Pressure coefficient
P	pressure	C_d	Discharge coefficient
W	Building width	C_d^*	Adaptive discharge coefficient
Q	Airflow rate	g	Acceleration of gravity
Ao	Opening area	θ	Opening area reduction factor
Z	Vertical coordinate		

1. Introduction

In developed and developing countries building sector accounts for about 40% of total energy demand in cities [1, 2]. The potential of natural and wind-driven ventilation for energy saving [3, 4] and thermal comfort [5, 6] has been recognized as an effective strategy in modern and traditional buildings [7]. Natural ventilation has a complex mechanism [8], placing it in the subject of many studies during the past 50 years [9]. Wind-driven cross-ventilation is the most commonly type of the natural ventilation in which pressure difference across the building caused by wind imposes the airflow thorough the building openings [10].

Researches are mainly focused to understand the complex mechanism of the cross-ventilation [11-13], to develop theoretical and empirical models [14-16], and to provide details of the airflow parameters [17-21]. Wind tunnel measurement [22-24] and on-site measurement [25-27] are broadly employed to explore the mechanism of the cross-ventilation, but their applications are mainly limited to simplified building geometries. Analytical models and computational fluid dynamics (CFD) method, on the other hand, are relatively cheaper and easier to provide the cross-ventilation information in complex building geometries.

Analytical and semi-empirical methods to model the cross-ventilation include power balance [28], local dynamic similarity (LDSM) [15] and air flow network (AFN) models [29]. Power balance model, proposed by Kato [28], is developed based on the concept of stream tube, and preservation and dissipation of a jet kinetic energy through the opening and inside a building. In

this model, in contrast to the simplified orifice model, which is based on Bernoulli equation, the dynamic pressure of the jet is considered in an energy balance equation. The total pressure loss and mass flow rate through openings are correlated to each other in the power loss equation. Another model for evaluation of the cross-ventilation is the local dynamic similarity model (LDSM) introduced by Kurabuchi et al. [15]. This model is developed based on a fact that the cross-ventilation flow structure in the vicinity of an inflow opening creates dynamic similarity under the condition that the ratio of the cross-ventilation driving pressure to the dynamic pressure of the cross flow is consistent at the opening. They used a Large Eddy Simulation (LES) model to estimate the variation of pressure along the stream tube, crossing the openings of a model building, and introduced a non-dimensional pressure, which is a function of openings' position and wind direction. Using this developed model, they calculated the discharge coefficient of the building model opening for different wind angles and opening positions.

Eventually, airflow network model (AFN) [29] is developed based on the mass balance and Bernoulli's equation between different nodes connected via airflow components (linkage) such as windows and doors. In this model, the variable defined at each node is pressure while the linkage variable is the mass flow rate [30]. Even though the power balance and LDSM models provide more accurate results and also present detailed information of the fluid dynamics, these models never gain the popularity of simplified orifice-based models such as AFN. The simplified formulation of the orifice-based models makes them a good choice for integrating with the building energy models for realistic engineering applications. Furthermore, there are many resources in open literature regarding the input parameters to the orifice-based models which make their application easy although their accuracy for large openings remains a controversial issue.

The orifice equation for the airflow rate (Q) through a sharp-edged opening, which is used in AFN model, can be expressed as below:

$$Q = c_d A \sqrt{\frac{2\Delta P}{\rho}} \tag{1}$$

where c_d, A, and ρ are the discharge coefficient, opening area and air density, respectively. The value of pressure difference ΔP across the opening is usually expressed in the form of pressure coefficient:

$$c_P = \frac{P - P_o}{\frac{1}{2}\rho U_{ref}^2} \tag{2}$$

where U_{ref} and P_o are the free stream wind speed and pressure at a reference height. According to Karava et al. [31], the orifice-based equation for the wind-driven cross-ventilation is valid when the flow is in a fully-developed turbulent regime, the openings do not affect the pressure distribution over the envelope, the kinetic energy of the airflow fully dissipates in downstream of the inlet opening, and the pressure drop equals to the static pressure difference across the

opening. Results of the numerical and experimental studies show that these assumptions are not fully satisfied for the cross-ventilation in buildings. For instance, according to the works presented in [12, 13, 21, 32], not only does the kinetic energy of the entering jet penetrate inside the building, but also a noticeable amount of the kinetic energy can exit across the outlet opening.

In addition to the inaccuracy of the orifice-based models for the large openings due to the idealized Bernoulli's equation, there are other sources of discrepancy in these models such as the one associated with the input parameters as addressed in [33-38]. The input parameters (e.g. the discharge and pressure coefficients in addition to the velocity profile), according to Karava et al. [31], are coupled together and their interaction should be analyzed in detail for a suitable cross-ventilation design. These parameters depend on many factors, including the building and opening geometries, and the sheltering effect of the surrounding buildings [31].

As highlighted in [39], assuming a constant value for C_d can be a major source of error in the AFN model in cross-ventilation studies. The value of discharge coefficient is a function of different parameters, including the opening porosity and Reynolds (Re) number [31, 39], wind direction [40, 41], turbulence parameters [42], pressure difference across the openings [43], and building geometry. A variation of c_d was reported for a gable roof-sloped building model to vary from 0.74 to 0.9 and 0.6 to 0.71 for velocity ratios of 0.63 and 0.5 [31]. The variation of c_d was reported to be insignificant for the wind incidence angles less than 30 degrees, but its value was shown to drop rapidly to a minimum value of 0.1 for the wind incident angles between 30 and 90 degrees [43].

Pressure coefficient C_P is another input parameter for the orifice-based model, which is generally obtained by wind tunnel/full-scale measurements, and analytical correlations. c_P values obtained from the measurement datasets [44, 45] and analytical methods [46-48] are only available for some limited basic building shapes. A noticeable difference between C_P values obtained from different datasets is reported, especially when the local distribution of c_P and sheltering effect are taken into the account [34]. The high importance of considering the uncertainties in the wind-induced pressure coefficient is widely emphasized [38] and recognized to be related to the existence of a wide range of affecting parameters, including façade design specification, building geometry, opening position, sheltering effect by surrounding buildings, obstacles (e.g. trees), and stochastic wind characteristics (i.e. direction, speed, turbulence intensity) [49].

The uncertainty in the input parameters of the orifice-based models, and the assumptions made in its formulation indicate that its application for the cross-ventilation scenarios should be conducted with more caution. Obviously, Computational Fluid Dynamics (CFD) can provide more accurate results than orifice-based model, however, with a significantly higher computational cost, specifically when time-variant building energy simulation studies are deemed. Hence, the aim of this study is to improve the accuracy of the orifice-based model using a novel deterministic-statistical framework. To this end, an adaptive discharge coefficient is

defined in this study, which is a function of the openings' geometry and location. The proposed framework for the accuracy improvement of the orifice-based model is described at first, and then details of the CFD simulation setup, validation and utilized experimental measurements are provided. A database is then generated from a series of CFD simulations using the Latin hypercube sampling methods while the modified discharge coefficient of the orifice-based model is adapted from the generated database using meta-model approximations. Finally, the accuracy of the proposed methodology is discussed by comparing the results of the orifice-based model, which utilizes the adaptive discharge coefficient, with the CFD and experimental measurements for different openings configurations.

2. Methodology

2.1 Proposed Framework

The proposed methodology for the accuracy improvement of the orifice-based model is shown in Figure 1. The goal is to generate an adaptive correlation for the discharge coefficient (C_d) as a function of building geometry, and openings' dimension and position. Therefore, at the first step, a validated CFD model for the cross-ventilation through an isolated building with two openings on the opposite walls was developed based on an experimental measurement conducted by Tominaga and Blocken [13]. In the next step, a database for the airflow rate of the building model was generated using the validated CFD model setting by alteration of the building and openings geometrical parameters shown in Figure 2; the optimal Latin hypercube sampling technique [50], a modified model of the Latin hypercube sampling, was then used to generate the required population in this study.

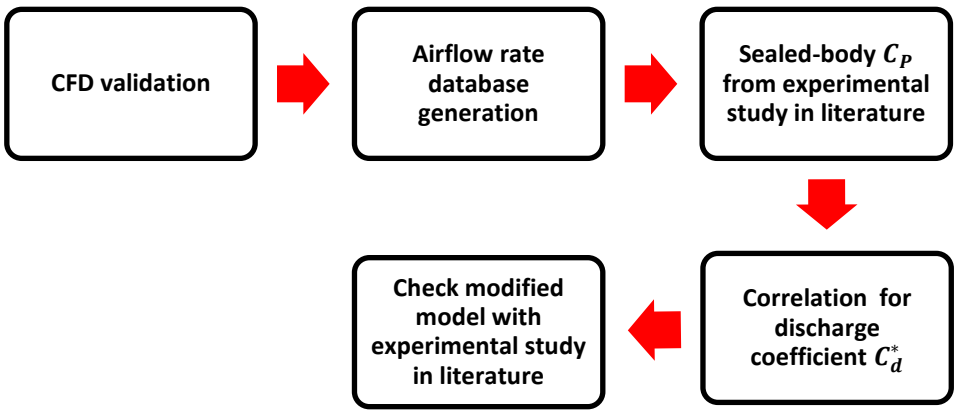

Figure 1 Procedure for development of the new correlation for the discharge coefficient

Once the database generation was completed, the airflow rate of each design case was passed into the orifice-based model. In addition, the local-surface wind pressure coefficient at the windward and leeward openings were obtained from a series of boundary layer wind tunnel

measurements deployed by Tamura [51]. Using the airflow rate from CFD and local surface wind pressure coefficient from the experiment, a new correlation for the discharge coefficient (C_d^*) was obtained as a function of the building geometry, and openings' dimension and location. The value of the modified discharge coefficient, assuming to be equal for the windward and leeward opening, is defined as follows:

$$C_d^* = \frac{Q_{CFD}}{U_{ref} A_{o1} \sqrt{C_{P1}^{Exp} - C_{Pi}}} \tag{3}$$

$$C_{Pi} = \frac{C_{P1}^{Exp} + \left(\frac{A_{o2}}{A_{o1}}\right)^2 C_{P2}^{Exp}}{1 + \left(\frac{A_{o2}}{A_{o1}}\right)^2} \tag{4}$$

where Q_{CFD} is the airflow rate predicted by CFD model while U_{ref}, A_{o1}, and A_{o2} are the free-stream velocity at a reference height and area of the windward and leeward openings, respectively. C_{P1}^{Exp} and C_{P2}^{Exp} are respectively the local-surface wind pressure coefficients at the windward and leeward openings obtained from the sealed-body measurement, and C_{Pi} is the internal pressure coefficient. The calculated modified discharge coefficient of each database sample was then used to create a meta-model approximation for C_d^* using response surface (RSM) and radial basis function (RBF) models. Finally, the accuracy of the orifice-based model with the modified discharge coefficient was examined by comparing the results with an available experimental study in literature.

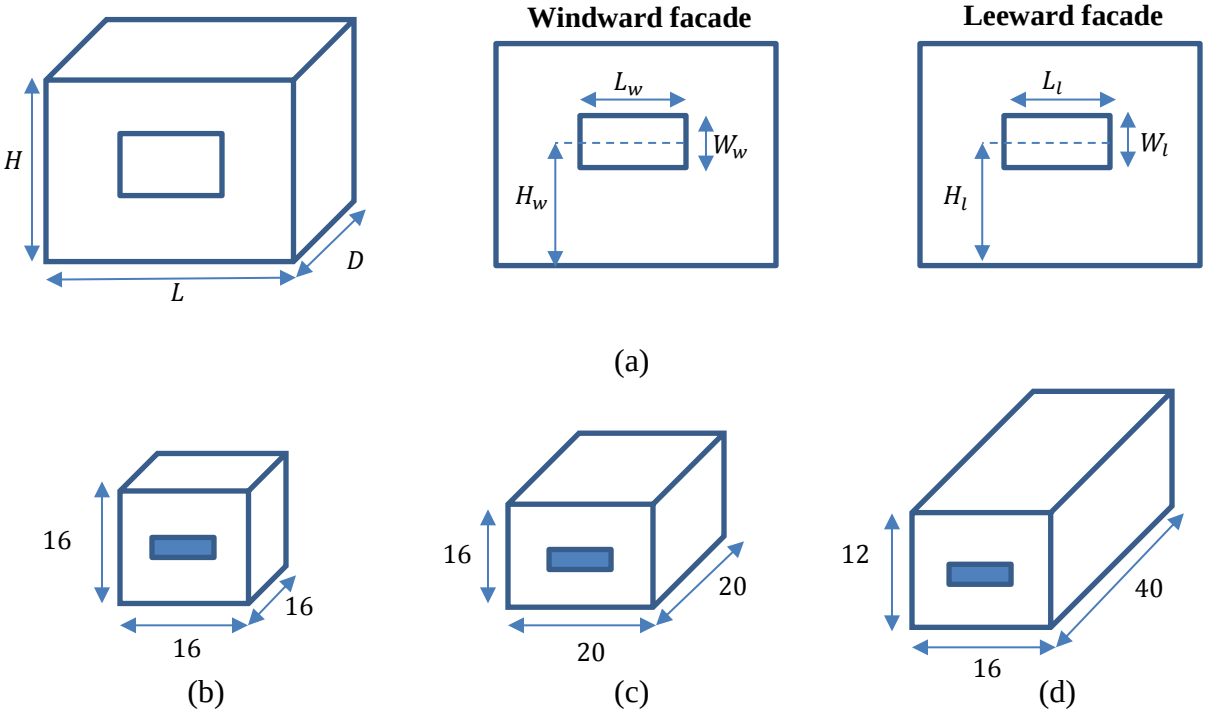

Figure 2 (a) Building geometry parameters for database generation. Dimensions of (b) square cube, (c) cuboid, and (d) long corridor building models

2.2 Database Generation

A schematic of the automatic database generation process for the cross-ventilation model is shown in Figure 3. The Statistics and Machine Learning Toolbox™ of MATLAB was used to generate design of experiments (DOE) samples. The geometry of the building (L, D, H), and the windward and leeward openings dimensions (L_w, L_l, W_w, W_l) in addition to their vertical positions (H_w, H_l) were passed to ANSYS DesignModeler in which a parametric geometrical model was created. The geometry of the building model was carried out to the ICEM CFD meshing package where a predefined mesh template was automatically applied. The created mesh was then handled in the CFX solver. After reaching an acceptable convergence, all output data, including airflow rate (Q) and parameters such as the opening Reynolds number (Re_o), opening velocity ratio (V_r) and flow Reynolds number, were automatically calculated and linked to MATLAB software. After the completion of the process, a meta-model was generated in MATLAB to produce a new adaptive discharge coefficient (C_d^*). Finally, the performance of the evolved meta-model was analyzed using a cross-validation method. Simulations were conducted using an 8-core AMD® CPU processor which took about 36 hours for each building geometry.

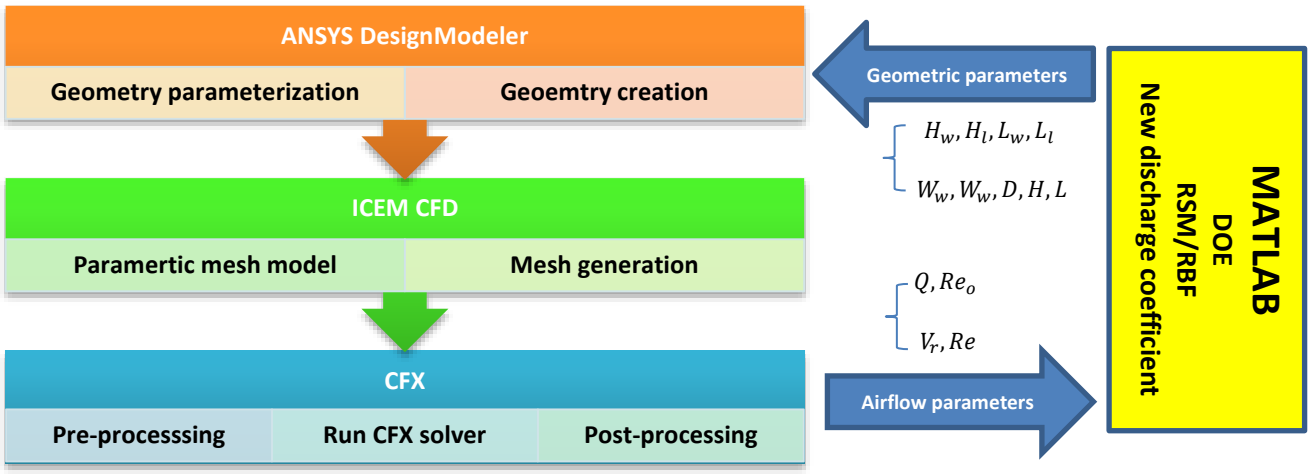

Figure 3 A schematic of the automatic database generation for cross-ventilation models

Three different building configurations were considered in this study adapted from the literature where experimental data were available, representing 1:100 scale models of buildings with full-scale dimensions of $L \times D \times H = 16 \times 16 \times 16\, m^3$, $L \times D \times H = 20 \times 20 \times 16\, m^3$, and $L \times D \times H = 16 \times 40 \times 12\, m^3$. As shown in Figure 2, the first building model is a square cube while the second and third models are cuboids. The third building has a large depth to breath ratio of 5:2, which represents a long corridor cross-ventilation scenario. The considered range for the opening dimensions and position are shown in Table 1. The wall porosity (P_r) variation for windward and leeward openings is in the range of $3\% \leq P_r \leq 25\%$ for all building models; in this range, the accuracy of the orifice-based model

found to be reasonable. The minimum distance between the openings and floor/roof edges is $0.1H$; both openings have equal distances from the side walls.

Table 1 Range of the openings dimensions for the database generation

	Square cube	Cuboid	Long corridor
Opening length	$L_{min} = 3.75$ $L_{max} = 12$	$L_{min} = 5$ $L_{max} = 16$	$L_{min} = 3.75$ $L_{max} = 12$
Opening width	$W_{min} = 1.94$ $W_{max} = 6.12$	$W_{min} = 1.94$ $W_{max} = 6.12$	$W_{min} = 1.45$ $W_{max} = 4.6$
Opening height	$H_{min} = 0.1H$ $H_{max} = 0.9H - W_{max}$	$H_{min} = 0.1H$ $H_{max} = 0.9H - W_{max}$	$H_{min} = 0.1H$ $H_{max} = 0.9H - W_{max}$

2.3 Design of the Computational Experiments

The accuracy of a meta-model is directly linked to the design of computational experiments or sampling methodology that is used for database generation process. Finding a proper space-filling methodology to decrease the number of required simulations is a challenging issue in design of computational experiments. In this study, the optimal Latin hypercube technique [50] was used to generate CFD samples of different openings dimensions and locations to create a meta-model for C_d^*. In the optimal Latin hypercube technique, the design space of each input parameter is first divided using a random Latin hypercube sampling to generate an initial DOE matrix. Then, an optimization technique, which is based on the enhanced stochastic evolutionary algorithm (ESE), is utilized to generate an even distribution of samples. The even distribution of samples is achieved by using an optimal criterion named the maximum distance criterion [52], which will be achieved if the minimum inner site-distance [50] is maximized:

$$\min_{1\le i,j\le n, i\ne j} d(x_i, x_j) \tag{5}$$

where $d(x_i, x_j)$ is distance between the sample points x_i and x_j defined as below:

$$d(x_i, x_j) = \left[\sum_{k=1}^{m} |x_{ik} - x_{jk}|^t\right]^{1/t} \quad t = 1 \text{ or } 2 \tag{6}$$

where n is the number of computational experiments (samples) and m is the number of factors (input parameters).

2.4 Approximation Techniques

Two different approximation techniques, including RSM and RBF model, were used in this study. In the RSM approximation, a series of low-order polynomials were used to approximate the behavior of the output responses. The model was trained using the samples generated from the CFD database. The number of samples required for the RSM development depends on the

polynomial terms (e.g. quadratic or cubic) [53]. In this study, the low-order Quadratic, Cubic, and Quartic models were used. The general form of a Quartic model is as follows:

$$\widetilde{F(x)} = a_0 + \sum_{i=1}^{N} b_i x_i + \sum_{i=1}^{N} c_{ii} x_i^2 + \sum_{ij(i<j)} d_{ij} x_i x_j + \sum_{i=1}^{N} e_i x_i^3 + \sum_{i=1}^{N} f_i x_i^4 \quad (7)$$

where N is the number of model inputs and x_i's are the model input samples. Constants a, b, c, d, e and f are the polynomial coefficients, which are calculated by solving a linear system of equations formed for each input sample. The RSM approximation generally gives reasonable prediction of the output response behavior over a small region around the input variables, but its accuracy is limited over the entire range of the input variables.

The second approximation technique used in this study is the RBF model, which is a type of neural networks technique and is used for the interpolation in multiple-dimensional spaces [54]. For given interpolation values $y_1, \dots, y_N$ at data locations $x_1, \dots, x_N$, the RBF model can be expressed as below [55]:

$$F(x) = \sum_{j=1}^{N} \alpha_j g_j(x) + \alpha_{N+1} \quad (8)$$

where $g_j(x)$ is a set of radial basis functions, e.g. Cubic splines:

$$g_i(x) = \|x - x_j\|^3 \quad (9)$$

The unknown coefficients α_j are obtained by solving a system of $N + 1$ equations as follows:

$$\begin{aligned} &\textstyle\sum_{j=1}^{N} \alpha_j g_j(x) + \alpha_{N+1} = y_i \quad i = 1, \dots, N \\ &\sum_{j=1}^{N} \alpha_j = 0 \end{aligned} \quad (10)$$

The accuracy of the RBF model is generally higher than the RSM; however, it requires considerably more samples for the training stage.

2.5 Experimental Setup for the CFD Validation

Results of the wind tunnel experiment conducted by Tominaga and Blocken [13] were used in this study for validation of the CFD model. In the experiment, a building model with dimensions of $0.2\,m \times 0.2\,m \times 0.16\,m$ ($L \times D \times H$) with two openings on opposite sides was placed in an atmospheric boundary layer wind tunnel at Niigata Institute of Technology. The split fiber probe (SFP) and constant temperature anemometry (CTA) module were used for the velocity measurement, and also the tracer gas method was utilized to measure the airflow rate. The length and width of the openings were $0.092\,m$ and $0.036\,m$, respectively. The experiment was performed for five different configurations with different opening positions as shown in Figure 4.

The time-averaged streamwise velocity and turbulent kinetic energy (TKE) at 63 measurement points inside the building model were further used to define validation metrics.

2.6 Experimental Setup for the Sealed-body Pressure Coefficient

In order to reduce the uncertainty of the orifice-based model due to the implementation of the surface-average C_P [56], the local value of C_P was used in this study rather than its mean value. The value of c_P was directly obtained from CFD simulations for the generated database; however, the accuracy of the Reynolds averaged Navier-Stokes (RANS) models in prediction of the wall surface pressure is relatively low [57, 58], and therefore it is not a common practice to find C_P [34]. Hence, in this study, the local distribution of C_P was adapted from a measurement by Tamura [51] in which wall pressure distributions over a flat-, gable-, and hip-roofed type of low-rise buildings were measured in a boundary layer wind tunnel. In Figure 5, the time-averaged distribution of C_P over windward and leeward surfaces of the building model with dimensions of $0.16\ m \times 0.16\ m \times 0.16\ m$ ($L \times D \times H$) is depicted.

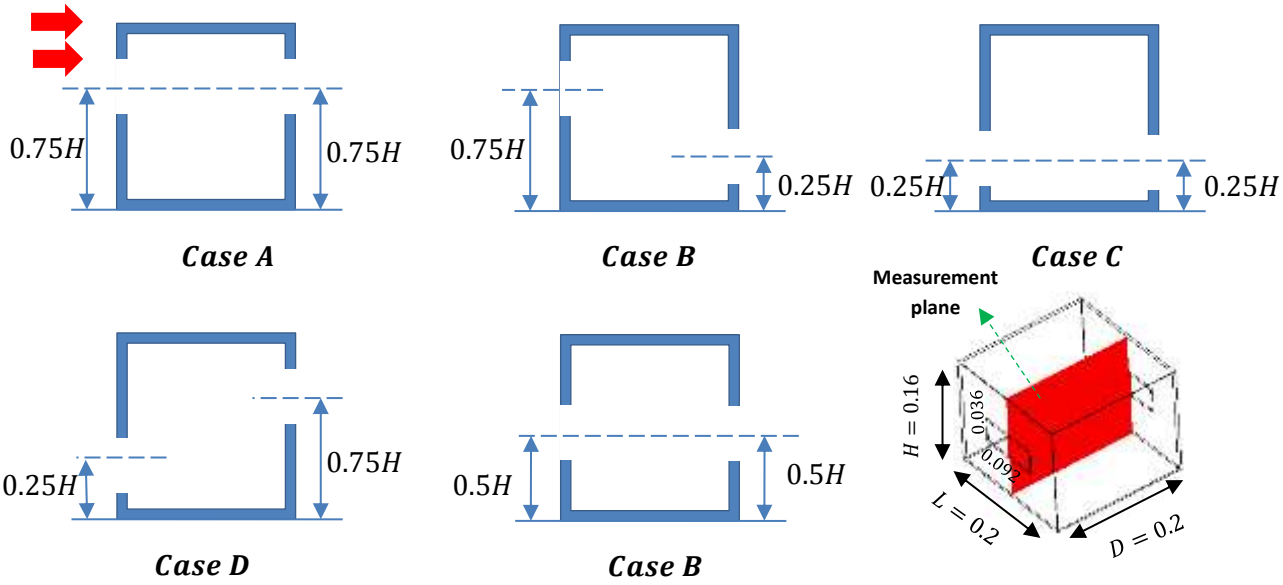

Figure 4 Vertical cross-section of the measurement configuration [13] utilized for the CFD validation

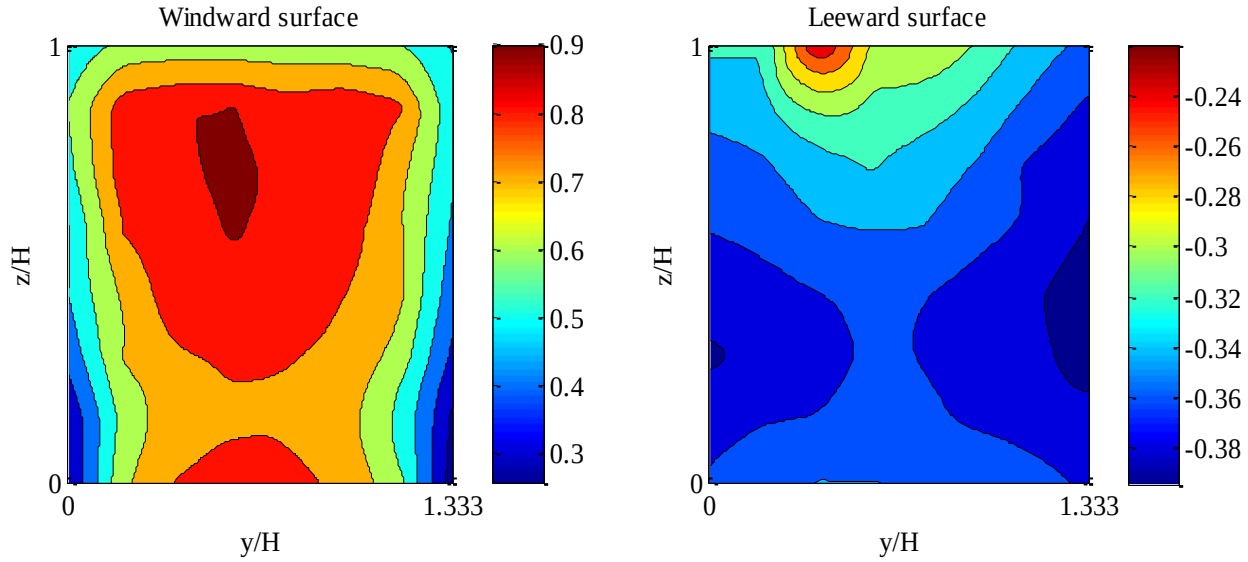

Figure 5 Contours of C_P from a wind tunnel measurement by Tamura [51] over (a) windward and (b) leeward surfaces

2.7 Mathematical Modeling

2.7.1 CFD Model

The 3D steady Reynolds averaged Navier-Stokes (RANS) equations were used to simulate the airflow around and inside the building model. The RANS equations can be derived by substituting mean and fluctuating components of the airflow variables into the Navier-Stokes equations. The air is considered to be incompressible, which is reasonable for atmospheric boundary layer (ABL) flows [59], so the mass and momentum equations are:

$$\frac{\partial(U_j)}{\partial x_j} = 0 \tag{11}$$

$$\rho U_j \frac{\partial U_i}{\partial x_j} = -\frac{\partial P}{\partial x_i} + \frac{\partial}{\partial x_j}\left(\mu_l \left[\frac{\delta U_i}{\delta x_j} + \frac{\delta U_j}{\delta x_i}\right] - \rho\overline{u_i u_j}\right) + S_{M_i} \tag{12}$$

where U and u are the average velocity and fluctuating velocity vectors, respectively. μ_l is the molecular viscosity and S_{M_i} is the sum of the body forces. Different turbulence models, including the standard $k-\varepsilon$, SST, $RNG\ k-\varepsilon$, $k-\omega$ and BSL Reynolds stress model ($BSL\ RSM$), were used in the conducted CFD simulations.

2.7.2 Air Flow Network (AFN) Model

In this study, performance of the cross-ventilation is calculated using the airflow network model embedded in EnergyPlus software. Influential parameters on the airflow components such as openings, doors, and cracks are considered as a series of linkages that connect nodes in different building zones [30]. The accuracy of the AFN model highly dependents on the wind pressure distribution around the building and the discharge coefficient of the openings. EnergyPlus

encompasses some internal correlations for the surface-averaged C_P, which are based on [48] for low-rise and [60] for high-rise buildings. It is also possible to enter user-defined values for C_P. Detailed description of the AFN model is provided in [29, 61]. A brief mathematical modeling description of the cross-ventilation in AFN is presented in the below equations; the total pressure difference (ΔP_t) between nodes n and m can be calculated by Bernoulli's equation [30]:

$$\Delta P_t = \left(P_n + \frac{\rho V_n^2}{2}\right) - \left(P_m + \frac{\rho V_m^2}{2}\right) + \rho g(z_n - z_m) \tag{13}$$

where P_n and P_m are the static pressure at nodes n and m, and V_n and V_m are the velocities at these nodes. ρ is the air density while z_n and z_m denote the nodes elevation. The mass flow rate for a one-way opening can be also calculated based on the orifice model as follows:

$$\dot{m} = C_d \theta \int_{z=0}^{z=H} \sqrt{2\rho\big(p_n(z) - p_m(z)\big)} W dz \tag{14}$$

where θ and W are the area reduction factor and opening width, respectively.

For a simple cross-ventilation scenario with two openings on the building walls, the opening velocity ratio may be calculated by [42, 62]:

$$\frac{U_1}{U_{ref}} = \frac{Q}{U_{ref} A_{o1}} = C_{d1} \left[\frac{A_r^2 C_{dr}^2}{1 + A_r^2 C_{dr}^2} |C_{P1} - C_{P2}|\right]^{1/2} \tag{15}$$

$$\frac{U_2}{U_{ref}} = \frac{Q}{U_{ref} A_{o2}} = C_{d2} \left[\frac{|C_{P1} - C_{P2}|}{1 + A_r^2 C_{dr}^2}\right]^{1/2} \tag{16}$$

where U_1 and U_2 are respectively the average velocity at windward and leeward openings and Q is the crossing airflow rate. A_r is the ratio of the openings area, $A_r = \frac{A_{o2}}{A_{o1}}$, and C_{dr} is defined as the ratio of the discharge coefficients $C_{dr} = \frac{C_{d2}}{C_{d1}}$. C_{P1} and C_{P2} are the wind surface pressure coefficients for the windward and leeward openings, respectively. Moreover, the internal pressure coefficient can be calculated as below:

$$C_{Pi} = \frac{C_{P1} + A_r^2 C_{dr}^2 C_{P2}}{1 + A_r^2 C_{dr}^2} \tag{17}$$

The reference wind speed at the local height (z) can be expressed as:

$$U_{ref} = U_{met} \left(\frac{\delta_{met}}{z_{met}}\right)^{\alpha_{met}} \left(\frac{z}{\delta}\right)^{\alpha} \tag{18}$$

where z_{met} is the height of the standard meteorological wind speed measurement. α and δ are the velocity profile exponent and boundary layer thickness, respectively, depending on the terrain type [30]. The wind surface pressure relative to the static pressure in an undistributed flow can be also determined by:

$$P_w = C_P \rho \frac{U_{ref}^2}{2} \tag{19}$$

2.8 CFD Simulation Setup, Computational Domain and Boundary Conditions

The RANS equations were solved using the commercial software ANSYS CFX and utilizing an element-based finite volume discretization method. The pressure-velocity coupling was based on the Rhie-Chow interpolation by Rhie and Chow [63] while a co-located grid layout was further implemented. The High Resolution Scheme was used for discretization of the advection terms while tri-linear shape functions were used to evaluate the spatial derivatives of the diffusion terms. For the near-wall treatment, the automatic wall function formulation [64] was adapted for the SST, $k-\omega$, and $BSL\ RSM$ models while the scalable wall function method was utilized for the $k-\varepsilon$ and RNG models. The convergence was set to be less than 10^{-5} for all variables.

A rectangular computational domain, as shown in Figure 6, was created for the CFD simulation based on the recommendations by AIJ guidelines [65] and [21, 66]. The domain width, length, and height were $2.12\,m \times 3.28\,m \times 0.96\,m$, respectively. Moreover, ICEM CFD was used to create a structured hexahedral mesh around and inside the building model. An O-grid block with first-layer size of $1 \times 10^{-4}\,m$ was used for the solid walls, resulting to an average $y^+ \approx 1$. No-slip boundary condition was considered for all solid walls with aerodynamically smooth surfaces. The symmetric wall boundary condition was also applied to the lateral and top boundaries, and a zero static pressure was assigned to the outlet plane. The inlet vertical velocity in addition to the turbulent kinetic energy profiles were adapted from the experiment by Tominaga and Blocken [13] (see Figure 7) to mock the condition at the lower part of a neutral atmospheric boundary layer:

$$\frac{U(z)}{U_H} = \left(\frac{z}{H}\right)^{0.25} \tag{20}$$

where $U(z)$ is the streamwise velocity at the height of z, and $U_H = 4.3\ {}^{m}/_{s}$ is the reference velocity at the building height H. The measured vertical profile of the TKE was also approximated by an exponential formulation [13] while the turbulent kinetic energy dissipation rate $\varepsilon(z)$ was approximated in accordance with the AIJ guidelines [65]:

$$\frac{k(z)}{{U_H}^2} = 0.033\ exp^{-0.32({}^{z}/_{H})} \tag{21}$$

$$\varepsilon(z) = {C_\mu}^{\frac{1}{2}} k(z) \frac{U_H}{H} \alpha \left(\frac{z}{H}\right)^{\alpha-1} \tag{22}$$

where $C_\mu = 0.09$ denotes the model constant and $\alpha = 0.25$.

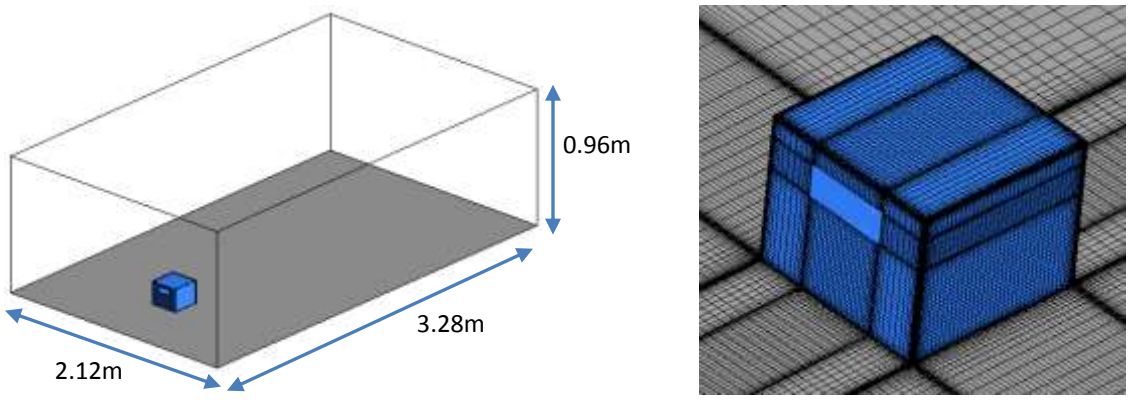

(a) (b)

Figure 6 (a) Computational domain and (b) computational grid around the building surfaces.

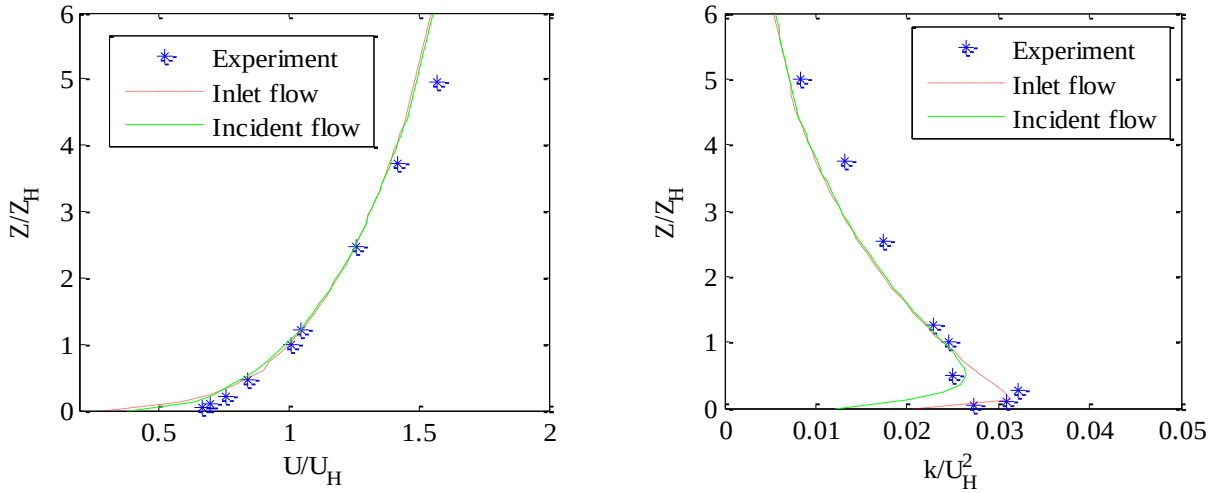

(a) (b)

Figure 7 Vertical profiles of (a) the time averaged velocity and (b) turbulent kinetic energy of the experiment for the inlet flow and the incident flow in an empty-domain test case

3. Result and Discussion

3.1 Mesh Independency Study

In order to find an independent mesh from the cell sizes, a sensitivity analysis was firstly conducted with three different cell numbers of 668,050; 1,231,824; and 2,271,371. Building configuration of case B (see Figure 4) was selected for the mesh independency study. In Figure 8, the profiles of the streamwise velocity are shown on the vertical plane at $\frac{x}{D} = 0.125$, $\frac{x}{D} = 0.5$, and $\frac{x}{D} = 0.875$. It can be seen that the difference between the fine and medium meshes is negligible, thus the later mesh was chosen for the rest of the CFD simulations in this study.

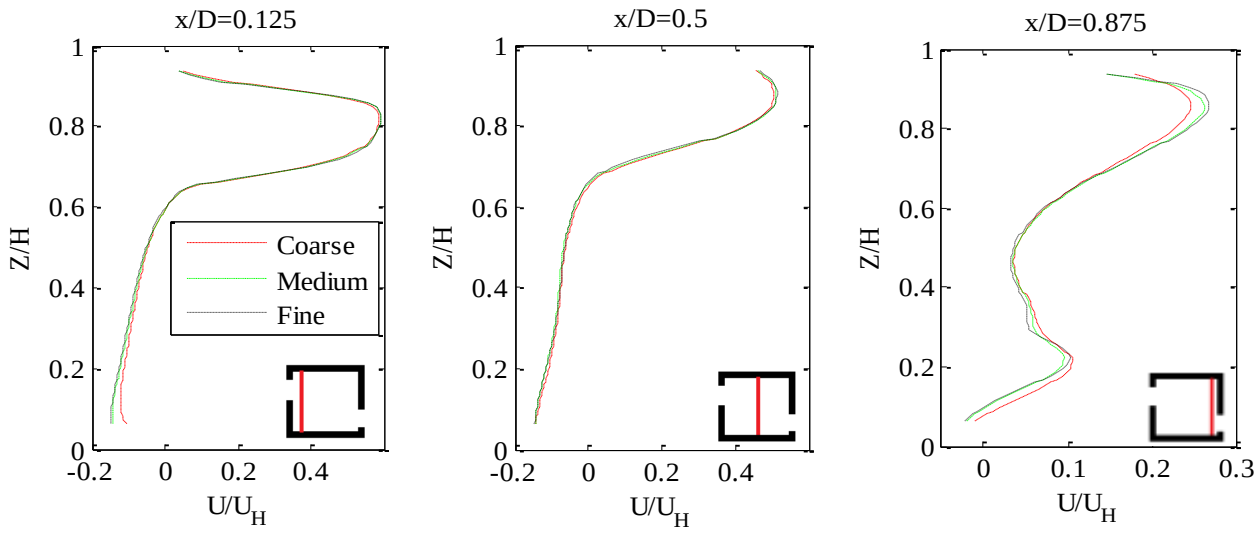

Figure 8 Vertical profiles of the streamwise velocity on the vertical plane at (a) $x/D = 0.125$, (b) $x/D = 0.5$, and (c) $x/D = 0.875$.

3.2 CFD Validation

For the validation study, performance of five commonly used turbulence models, including the standard $k-\varepsilon$, $RNG\ k-\varepsilon$, $k-\omega$, SST and $BSL\ RSM$, were compared in terms of airflow rate and validation metrics for the velocity field.

3.2.1 Airflow Rate

As shown in Figure 9, the CFD predictions of the non-dimensional airflow rate ($\frac{Q}{A_o U_H}$) for different opening configurations and turbulence models are compared with the experimental results by Tominaga and Blocken [13]. It can be seen that the airflow rate demonstrates a relationship with the openings height. The highest experimentally measured airflow was reported for Case A where both windward and leeward openings are placed at the upper half of the building height close to the roof. Inversely, the lowest airflow rate was measured in cases C and D where the windward opening is close to the ground. The windward opening in case A is located near the stagnation point of the building, exposing to a higher wind surface pressure and free stream velocity, and therefore resulting in a higher airflow rate. In contrast, for cases C and D, not only the wind surface pressure around the windward opening is low, but the entering velocity is also low due to the lower height of the windward opening; hence, these cases correspond to the lowest airflow rates.

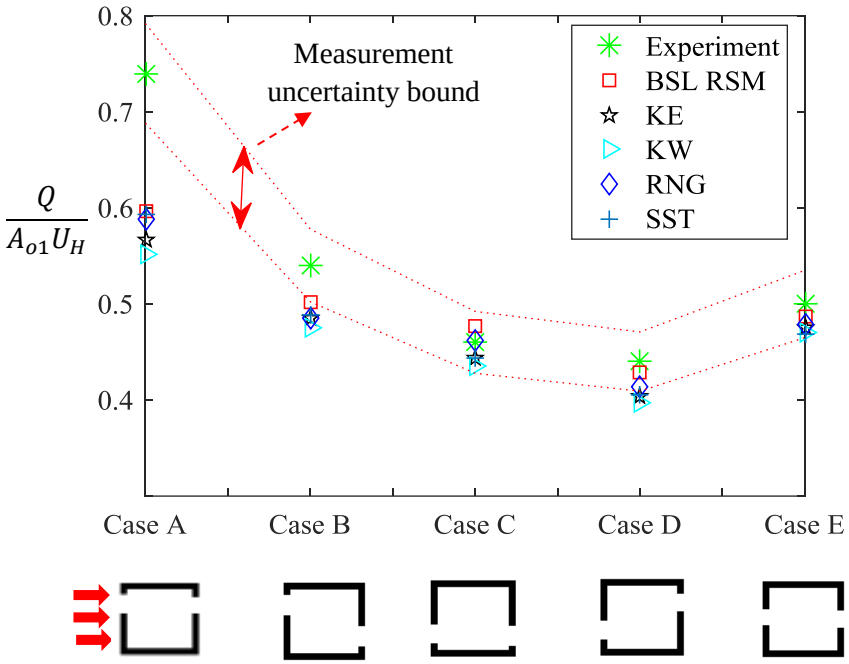

Figure 9 Airflow rate prediction by CFD models in comparison with the experimental results by Tominaga and Blocken [13]

In order to compare the CFD and experimental results, the lower and upper bounds of the measured airflow rate are also depicted in Figure 9, which are obtained based on a $\pm 7\%$ uncertainty of the tracer gas method reported by [13]. Comparing the airflow rate predictions by CFD and those of the measurement reveals that the accuracy of all turbulence models are acceptable for cases C, D, and E as the predicted values are within the upper and lower bounds. Nonetheless, for cases A and B, where windward opening is located at the upper height of the building near the stagnation point, the calculated airflow rate with all turbulence models are out of the expected range of the experiment. The relative error in prediction of the airflow rate for case A is about 20% for the $BSL\ RSM$, RNG, and SST models and 23% and 25% for the standard $k-\varepsilon$ and $k-\omega$ models, respectively.

For case B, the relative error for the standard $k-\varepsilon$, $k-\omega$, SST and RNG models is about 10% while the $BSL\ RSM$ shows the lowest error of about 7%. The low accuracy of the RANS models in prediction of the airflow rate for cases A and B is associated to the poor accuracy of the steady RANS models in estimation of the flow behavior in the stagnation point over the windward façade. Moreover, incapability of the steady RANS models in prediction of the unsteady behavior of the flow around the building and the entering jet near the windward opening inside the building results in a lower accuracy for the CFD models of cases A and B. As demonstrated in [13], the flapping behavior and the Kelvin–Helmholtz instability formation are very strong in cases A and B, which cannot be captured by the steady RANS models. In contrast, the flapping behavior of the entering jet and the Kelvin–Helmholtz instability are noticeably decreased in

cases C and D where the windward opening is closer to the floor, and hence, more accurate CFD predictions are obtained for these two cases.

3.2.2 Velocity Field

Vertical profiles of the streamwise velocity U/U_H on the vertical plane at streamwise positions $x/D = 0.125$ and $x/D = 0.875$ close to the windward and leeward openings are illustrated in Figure 10. Numerical results for all opening configurations are compared with the experimental results by Tominaga and Blocken [13]; for case E, the numerical results are also compared with the numerical results by van Hooff, Blocken and Tominaga [21]. For case A, in which both openings are located at the upper half of the building height close to the roof, the entering jet through the windward opening has the maximum velocity ratio of $U_{max}/U_H = 0.75$. The jet momentum is weakened as it moves toward the leeward opening where the jet velocity ratio becomes $U_{max}/U_H = 0.45$. For case A, all turbulence models present acceptable results for the vertical velocity profiles. The SST and RNG models, however, over-predict the jet velocity at the windward and leeward openings, and under-predict the recirculation flow at the middle of the building surface close to the windward opening. The velocity of the entering jet for case B is $U_{max}/U_H = 0.5$, which is apparently lower than the case A, despite having the same height for the windward opening. In case B, as demonstrated in [13], the airflow encounters a larger resistance inside the building in comparison with case A, because the entering jet impinges on the opposite wall, and then redirects toward the leeward opening near the floor. In this case, the outlet jet velocity ratio is noticeably decreased to $U_{max}/U_H = 0.11$. This implies the reason for the higher airflow rate for case A, which is 1.4 times larger than the one measured in case B. The accuracy of all turbulence models is observed to be reasonable for case B; however, they all overestimate the recirculating flow close to the floor at $x/D = 0.125$.

For case C, the entering jet has a lower velocity than cases A and B. This is mainly due to the lower pressure difference across the openings, and also the lower velocity at the opening height in comparison with cases A and B. The measured jet velocity for this case is about $U_{max}/U_H = 0.4$, but all CFD models over-estimate the value between 0.5 and 0.6. The estimated streamwise velocity profile by the RANS models is generally very close to the experiment. A same outlet jet velocity about $U_{max}/U_H = 0.25$ is obtained by all turbulence models similar to the experiment. Case D has almost a same entering jet velocity as case C, but the outlet jet has a considerably lower velocity of $U_{max}/U_H = 0.1$ as the flow is directed upward to the leeward opening. The accuracy of the CFD model is acceptable though it underestimates the velocity profile of the recirculating flow at the upper height section.

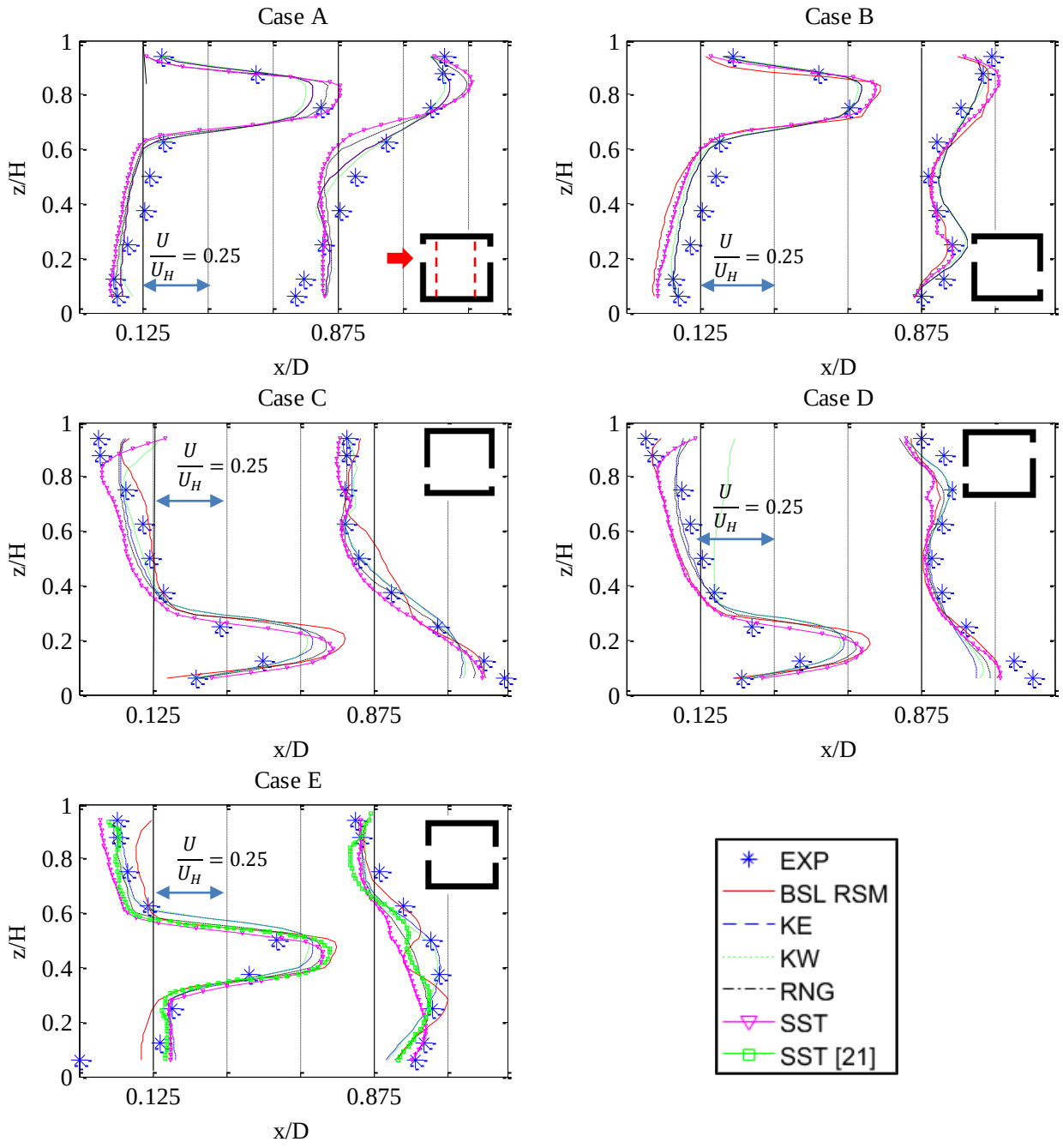

Figure 10 Vertical profiles of the streamwise velocity on the vertical plane at $x/D = 0.125$ and $x/D = 0.875$ for different turbulence models.

The measured velocity jet for case E with two openings at the mid height of the building was reported to be about 0.43, but it is again overestimated by all turbulence models in a range between 0.50 and 0.58. At the leeward opening, the velocity is decreased to a half value predicted in the windward jet. Numerical results provided by van Hooff, Blocken and Tominaga [21] are also depicted for the *SST* turbulence model, which is again very close to the simulation results. The velocity vector near the leeward opening is generally under-predicted by the *SST* and *RNG* models.

In order to have more precise view on the accuracy of the CFD model, the fraction of the predictions within a factor of 2 of the observations ($FAC2$) are calculated for the velocity field over the 63 measurement points inside the building (see Figure 4). The *FAC2* metric is defined as below:

$$FAC2 = \frac{1}{N}\sum_{i=1}^{N} n_i \quad if \quad 0.5 \leq \frac{P_i}{Q_i} \leq 2 \quad n_i = 1 \quad else \quad n_i = 0 \tag{23}$$

where Q_i and P_i are the measured and computed values of the streamwise velocity for sample i, respectively. $N = 63$ is the number of measurement points. The ideal value for a complete agreement between the experiments and numerical results is $FAC2 = 1$.

As shown in Table 2, for all turbulence models and opening configurations, the value of $FAC2$ is larger than the threshold of $FAC2 \geq 0.5$ [67]. The highest agreement between the CFD and experimental results is obtained for cases C and D with $FAC2 > 0.7$ against all turbulence models except the $BSL\ RMS$ for case D where $FAC2 = 0.62$. The accuracy of the CFD model in prediction of the velocity profile for cases A, B and E shows almost same values; however, as shown in Figure 9, the accuracy of the CFD model in estimating the airflow rate was beyond the measurement uncertainty in cases A and B.

Table 2 Validation metrics for the streamwise velocity ($\frac{U}{U_H}$) for different turbulence models

$FAC2$	Case A	Case B	Case C	Case D	Case E
$BSL\ RSM$	0.57	0.54	0.70	0.62	0.57
$k-\varepsilon$	0.65	0.68	0.84	0.78	0.68
$k-\omega$	0.71	0.67	0.81	0.70	0.68
RNG	0.58	0.68	0.86	0.76	0.60
SST	0.60	0.57	0.73	0.71	0.57

3.3 Variation of the Airflow Rate for Different Building Configurations

In Figure 11, the variation of the non-dimensional airflow rate through the windward opening, average internal pressure coefficient (C_{Pi}), and the local pressure difference between windward and leeward openings ($\Delta C_P = C_{P1}^{Exp} - C_{P2}^{Exp}$) are plotted for five different opening positions defined as cases A, B, C, D and E, and three building configurations (i.e. square cube, cuboid, and long corridor). The relative position of the windward and leeward openings is also shown in Figure 4.

For the square cube and cuboid buildings, the highest airflow rate is achieved in case A (Fig.11_a) where the mean internal pressures are lower than other cases; the local wind surface pressures, however, are higher. For all three building models, when the leeward opening is

located close to the ground (case B), the mean internal pressure noticeably increases while the wind surface pressure inversely decreases, and thus the airflow rate decreases relative to case A.

For cases C and D, in which the windward opening is located close to the ground, the airflow rate further decreases. In these cases, despite having the lowest internal pressure, the free stream velocity is significantly lower at the windward opening height. Furthermore, the wind surface pressure is noticeably lower than other cases (see Fig.11_c). Comparing to cases C and D, the airflow rate increases in case E for all three building models while the internal and wind surface pressures elevate as well. The trends of the airflow rate variation for the square cube and cuboid buildings are very similar, but the long corridor model is quite less sensitive to the openings position. This is mainly due to the lower wind surface pressure gradient over the windward and leeward surfaces of this building model (Fig.11_c).

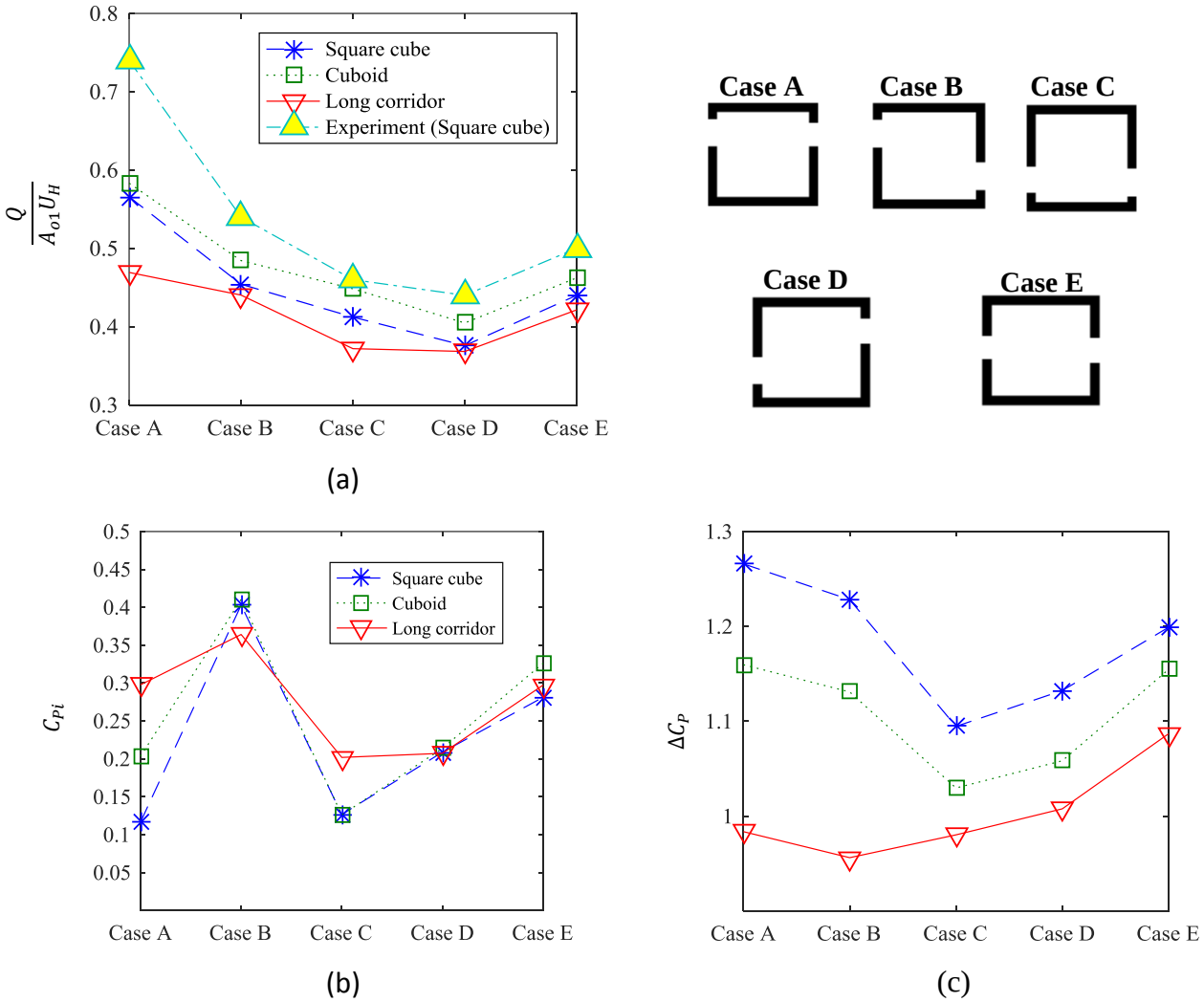

Figure 11 Effect of the openings position and building geometry on (a) the non-dimensional airflow rate at the windward opening (b) the mean internal pressure (c) the local wind surface pressure difference.

3.4 Factor Screening for Fitting the Model Approximation for C_d^*

A total number of 250 samples (CFD simulations) were generated for each building model (i.e. square cube, cuboid, and long corridor buildings) using the methodology that was described in Figure 3. In Figure 12, the histogram of the adaptive discharge coefficient (C_d^*) for the square cube, cuboid and long corridor buildings is shown. The values of C_d^* for the square cube and cuboid buildings are changing between $0.47 \leq C_d^* \leq 0.78$ and $0.41 \leq C_d^* \leq 0.83$, respectively. For the long corridor model, the C_d^* variation is smaller than the other building models with a value between 0.46 and 0.63. The mean value of C_d^* over 250 samples for each building model is also shown in Figure 12. These values for square cube, cuboid, and long corridor buildings are 0.57, 0.62, and 0.56, respectively. The standard deviation of C_d^* is respectively 0.05, 0.06, and 0.03 for square cube, cuboid, and long corridor buildings. It is evident that the long corridor building not only has the lowest mean value of C_d^*, but it also does have the lowest standard deviation.

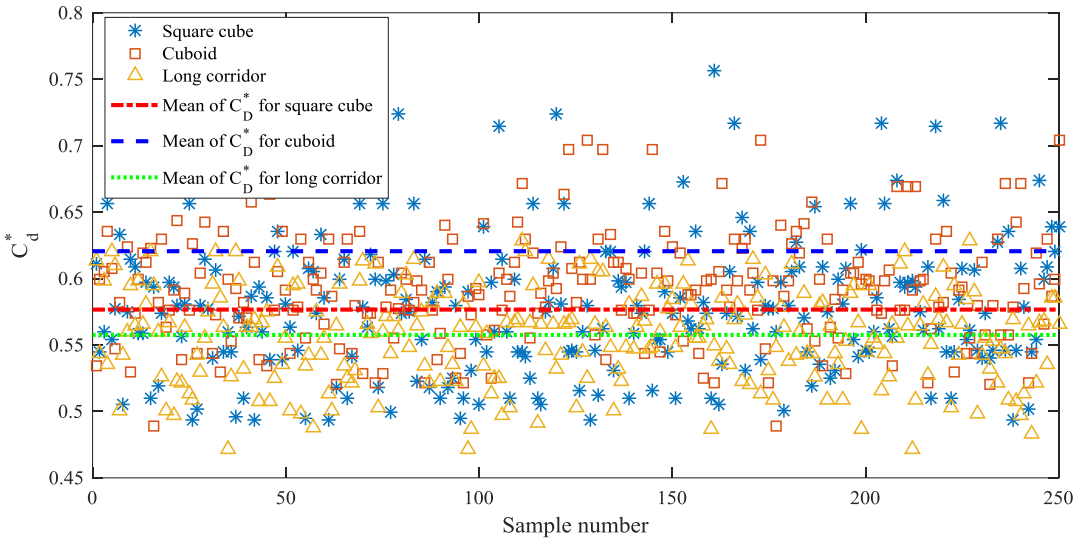

Figure 12 Histogram of discharge coefficent for square cube, cuboid, and long corridor building models.

The first step in fitting and analyzing the RSM for the adaptive discharge coefficient (C_d^*) is to identify factors that have the most influence on the variation of C_d^*. This process is called factor screening or characterization [68], and was performed for 250 samples for each building model. In Figure 13, the Pareto chart of standardized effects on C_d^* is shown for the square cube, cuboid and long corridor building models. The Pareto chart shows the relative magnitude and statistical significance of input parameters on the output response [69]. The reference line on the charts indicates which effects are significant; factors are considered significant when their effects are larger than the reference line. Thus, all the factors that have less effect than the reference line are considered insignificant.

As it can be seen in Figure 13, the effect of the windward and leeward openings position (H_w, H_l), geometry (L_w, L_l, W_w, W_w), and their 2nd- and 3rd-order correlations are considered in this

analysis. It can be observed that, for all building geometries, the most effective factor on the discharge coefficient is the vertical position of the windward opening (H_w). For the square cube and cuboid building shapes, the variation of the leeward opening position (H_l) has a significant effect on the C_d^* variation, but in contrast, for the long corridor building model, C_d^* is less sensitive to the leeward opening position. Correlation effects up to the 2nd-order are significant for the three building models, but all of the 3rd-order correlations are insignificant.

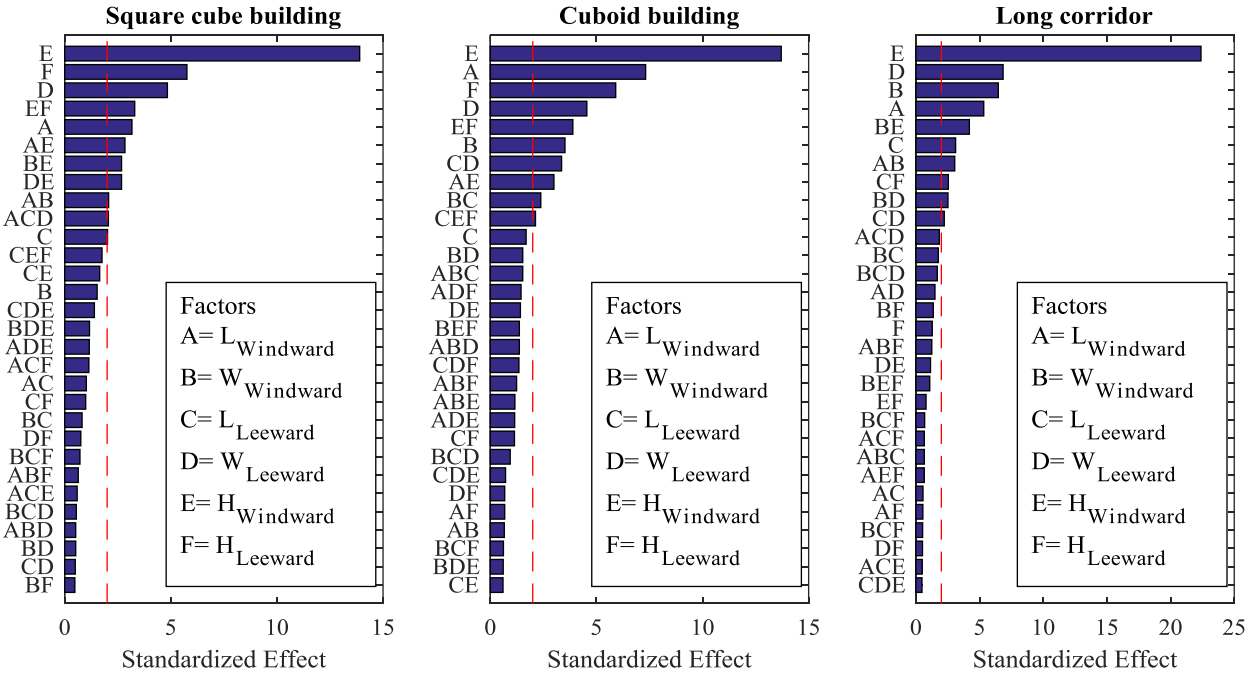

Figure 13 Pareto chart of standardized effects of C_d^* for (a) square cube, (c) cuboid, and (c) long corridor building models.

3.5 Results of the Cross-validation Study for Model Approximations of C_d^*

Using the results of the factor screening, three different RSM approximations based on the Quadratic, Cubic, and Quartic polynomial models were created for C_d^* for each building model. Furthermore, two model approximations based on the RBF networks, namely RBF1 and RBF2, were created, and their accuracies were compared with the RSM approximations. To this end, a cross-validation study for the cuboid building model was conducted using 30 samples randomly selected from 250 samples of the generated database. A fixed seed number was used in the cross-validation sampling to ensure that a fixed set of samples are always selected for the error analysis. Results of the cross-validation study are presented in Table 3. In the Quadratic model, a total number of 28 samples were used while 34 and 40 samples were respectively utilized in the Cubic and Quartic models. The required samples were determined based on the results of the factor screening study as explained before; only 2nd-order correlations were used in the RSM model. A total number of 90 and 220 samples were used for training of the RBF1 and RBF2 networks.

The average errors of the Quadratic and Cubic models are 0.074 and 0.071, respectively. The Quartic model shows an average-error of about 0.075. A lower average-error is obtained for the RBF models with a value of 0.064 and 0.054 for the models with 90 and 220 samples, respectively. The calculated maximum-error of all model approximations is very close to each other and is in the range of 0.41 to 0.44. The root-mean-square (RMS) errors of the Quadratic and Quartic models are equal to 0.107. The lowest RMS-error is predicted for the RBF2 model, which is about 0.098. It can be seen that, the RBF2 model provides the highest accuracy for the model approximation of C_d^*, hence, it was selected for creating the correlation for the adaptive discharge coefficient. Similar results were found for the square cube and long corridor building models. After tuning the obtained correlation and its individual terms, a final correlation for C_d^* was generated for each building model. The coefficients of the developed approximations for the adaptive discharge coefficient are available on request.

Table 3 Cross-validation study for model approximations of C_d^* over 30 samples

Model approximation	Number of training samples	Average error	Maximum error	RMS error
RSM Quadratic	28	0.074	0.423	0.107
RSM Cubic	34	0.071	0.416	0.106
RSM Quartic	40	0.075	0.412	0.107
RBF1	90	0.064	0.448	0.102
RBF2	220	0.054	0.443	0.098

3.6 Accuracy of the AFN Model for Adaptive Discharge Coefficient C_d^*

The accuracy of the proposed model is investigated with comparing the airflow rate prediction by the modified orifice-based model and CFD simulation for 30 cross-validation samples, which were not initially used in the RSM and RBF models development. As shown in Figure 14, for each sample, three different errors corresponding to the airflow rate are defined, including (1) the surface-averaged wind pressure with constant discharge coefficient of $C_d = 0.6$, (2) the local-surface wind pressure with constant discharge coefficient of $C_d = 0.6$, and (3) the local-surface wind pressure with adaptive discharge coefficient (C_d^*). For the square cube and long corridor building models, the relative errors with the constant C_d and surface-averaged wind pressure vary between -19.0% and 19.4%, and -12.5% and 12.7%, respectively. The corresponding errors for the cuboid building model change in a narrower range between -2.4% and 14.3%. For the case with the constant C_d and local-surface wind pressure, the minimum and maximum errors are -28.7%, -11.3%, -21.4%, and 10.8%, 5.5%, 1.6% for square cube, cuboid, and long corridor building models, respectively. For the long corridor building model, the relative error for most samples using local-surface wind pressures and constant C_d is negative, which means that the airflow rate is under-predicted by the orifice-based model. For this scenario, the local gradient of

the surface wind pressure on the windward and leeward surfaces is not as high as those for other two building models. Thus, using the local-surface wind pressure instead of the surface-averaged wind pressure does not improve the accuracy of the orifice-based model.

When the orifice-based model is used with the local-surface wind pressure and adaptive discharge coefficient (C_d^*) as a function of the openings' geometry and position, the relative error of the airflow rate is seen to be considerably lower than the cases with constant C_d. The minimum and maximum errors of the airflow rate with the adaptive discharge coefficient using the RBF2 correlation for the square cube, cuboid and long corridor buildings are found to be -5.8%, -4.9%, -1.2% and 8.8%, 4.8%, 1.2%, respectively. This apparently shows that assuming a constant discharge coefficient for the cross-ventilation scenarios considerably decreases the accuracy of the orifice-based equation for the wall porosity range between 3% and 25%.

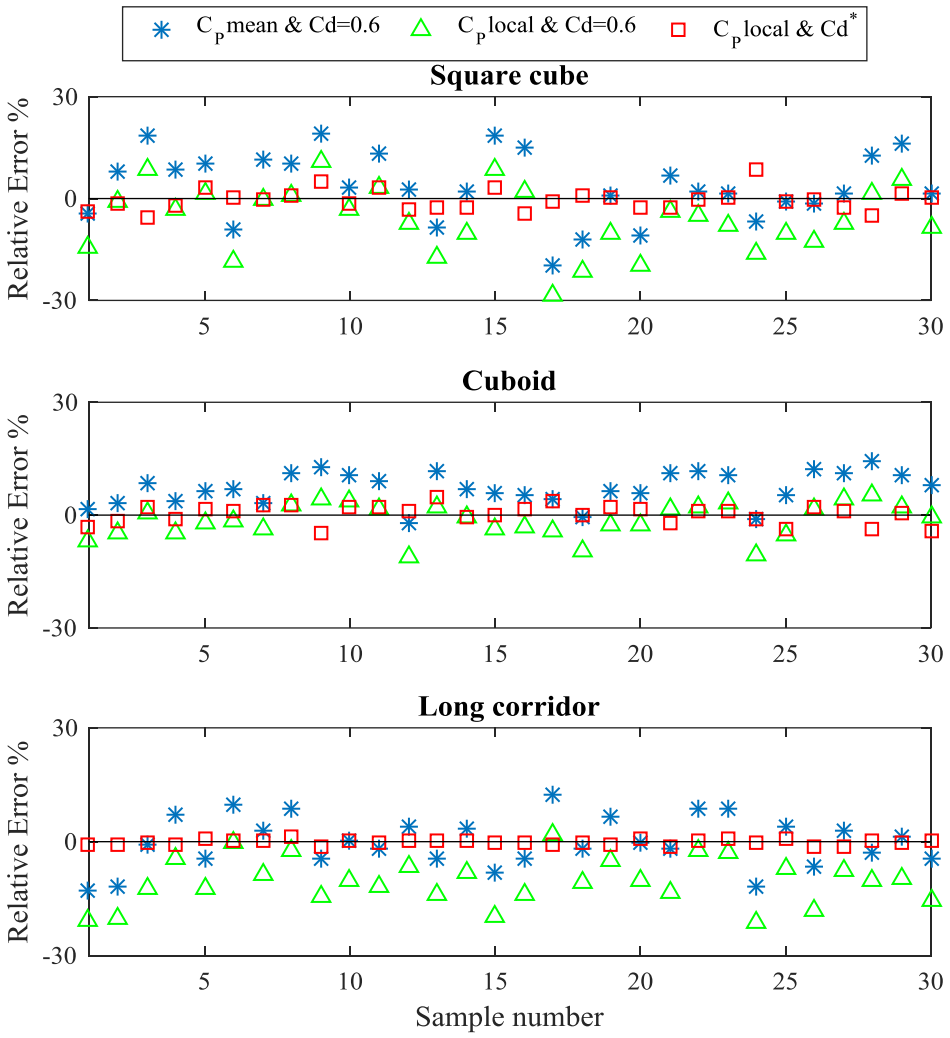

Figure 14 Relative error of the airflow rate of the orifice-based equation for different opening configurations.

The relative errors of the airflow rate calculated by the modified orifice-based equation for cases A, B, C, D and E compared to the experimental results by Tominaga and Blocken [13] are plotted in Figure 15. For all opening configurations, the relative error of using the surface-averaged wind pressure and constant C_d is larger than those obtained from the local-surface wind pressure; the values are found to be 45.5%, 25.4%, 12.4%, 8.4% and 19.4% for cases A, B, C, D and E, respectively. The relative error of the orifice-based equation with the local-surface wind pressure and constant C_d is estimated to be 38.3%, 16.5%, 6.4%, 0.8%, and 8.8% for cases A, B, C, D and E, respectively. The CFD simulation error for all cases except case D is found to be less than those estimated with using the local-surface wind pressure and constant discharge coefficient.

When the local-surface wind pressure with the adaptive discharge coefficient is used in the orifice-based equation, the error of the airflow rate estimation is considerably reduced to 22.8%, 8.1%, 3.3%, 7.4% and 7.3% for cases A, B, C, D and E, respectively. The significant increase in the accuracy of the orifice-based model using the adaptive discharge coefficient can be observed for all opening configurations in Figure 15. The highest value of C_d^* is obtained for case A where $C_d^* = 0.77$ followed by case B with $C_d^* = 0.66$. For cases C and E, the value of C_d^* is found to be 0.62 and 0.61, respectively. The lowest value of $C_d^* = 0.56$ is calculated for case C.

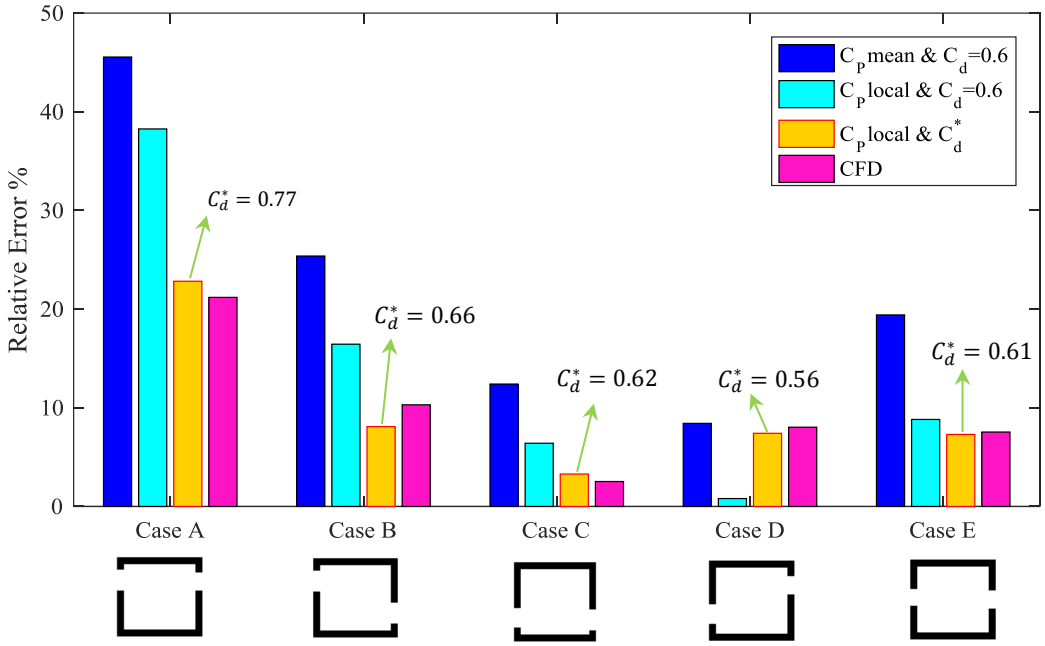

Figure 15 Relative error of the airflow rate calculation based on the orifice-based equation and CFD model for different opening configurations in comparison with the experiment by Tominaga and Blocken [13]

3.7 Conclusion

The application of the orifice-based model utilized in AFN model for the cross-ventilation of unsheltered building models was discussed for different building geometries and different opening configurations. It was shown that, assuming a constant value for the discharge

coefficient for the openings results in a noticeable inaccuracy of the orifice-based model in prediction of the airflow rate. A modified and adaptive discharge coefficient (C_d^*) was therefore proposed, which is a function of the building and openings geometries and vertical positions. The modified discharge coefficient was obtained by utilizing statistical methods and meta-model approximations for three different building configurations, including square cube, cuboid, and long corridor scenarios. A CFD model was, at first, validated using an experimental study, and then a database was generated for different opening positions by varying the building and openings' geometry and vertical position. The calculated airflow rate from the CFD model alongside the local-surface wind pressure from the experiment was passed into the orifice-based model to define the adaptive discharge coefficient. The accuracy of the proposed discharge coefficient correlation was discussed by comparing the airflow rate results with the CFD and experiment for a cuboid building model. The following findings can be addressed as the main conclusions of this study:

- The accuracy of CFD and the orifice-based models varies for different opening configurations; the highest discrepancy occurs when the windward opening is close to the roof with relative errors of 20% and 45.5% for the CFD model and the orifice-based model with surface-averaged wind pressure and constant discharge coefficient, respectively.
- The accuracy of the orifice-based model for the square cube and cuboid buildings can be improved by using the local-surface wind pressure instead of the surface-averaged wind pressure. However, the long corridor building model is less sensitive to the surface wind pressure gradient over the windward and leeward openings.
- The highest airflow rate can be obtained when the windward opening is close to the roof for the square cube and cuboid buildings. In contrast, for the long corridor building, the airflow rate variation with the opening positions is smaller than other building models.
- The accuracy of the orifice-based model can be considerably increased when the modified and adaptive discharge coefficient is used instead of a constant value, which is a default value in the AFN model embedded in EnergyPlus; the relative error of the airflow rate can be decreased from 38% to 22% for case A and from 16.5% to 8.0% for case B.

Despite the noticeable improvement shown in this study for the prediction of the cross-ventilation airflow rate, accuracy of the CFD and orifice-based model using the modified discharge coefficient is still lower than the measurement uncertainty when both windward and leeward opening are close to the roof (Case A and B). Further study, hence, is required to investigate the performance of the RANS models for the situations where the openings are close to the stagnation point on the windward façade. Future works will be focused to extent the proposed methodology for other wind angles and also to consider the sheltering effects.

Acknowledgment

The authors would like to express their gratitude to the University of Guilan for their financial support of this research.

References

[1] C.A. Balaras, A.G. Gaglia, E. Georgopoulou, S. Mirasgedis, Y. Sarafidis, D.P. Lalas, European residential buildings and empirical assessment of the Hellenic building stock, energy consumption, emissions and potential energy savings, Building and Environment 42(3) (2007) 1298-1314.
[2] H.-x. Zhao, F. Magoulès, A review on the prediction of building energy consumption, Renewable and Sustainable Energy Reviews 16(6) (2012) 3586-3592.
[3] K. Kumaran, Heat, air and moisture transfer in insulated envelope parts, Final report 3 (1996).
[4] B. Wang, T. Dogan, D. Pal, C. Reinhart, Simulating naturally ventilated buildings with detailed CFD-based wind pressure database, (2012).
[5] Z. Cheng, L. Li, W.P. Bahnfleth, Natural ventilation potential for gymnasia – Case study of ventilation and comfort in a multisport facility in northeastern United States, Building and Environment 108 (2016) 85-98.
[6] P. Prajongsan, S. Sharples, Enhancing natural ventilation, thermal comfort and energy savings in high-rise residential buildings in Bangkok through the use of ventilation shafts, Building and Environment 50 (2012) 104-113.
[7] Y.C. Aydin, P.A. Mirzaei, Wind-driven ventilation improvement with plan typology alteration: A CFD case study of traditional Turkish architecture, Building Simulation, Springer, 2017, pp. 239-254.
[8] P. Karava, Airflow prediction in buildings for natural ventilation design: wind tunnel measurements and simulation, Concordia University, 2008.
[9] D. Etheridge, A perspective on fifty years of natural ventilation research, Building and Environment 91 (2015) 51-60.
[10] N. Khan, Y. Su, S.B. Riffat, A review on wind driven ventilation techniques, Energy and Buildings 40(8) (2008) 1586-1604.
[11] M. Sandberg, Wind induced airflow through large openings: summary, International Energy Agency Annex 35 (2002).
[12] Y. Tominaga, B. Blocken, Wind tunnel experiments on cross-ventilation flow of a generic building with contaminant dispersion in unsheltered and sheltered conditions, Building and Environment 92 (2015) 452-461.
[13] Y. Tominaga, B. Blocken, Wind tunnel analysis of flow and dispersion in cross-ventilated isolated buildings: impact of opening positions, Journal of Wind Engineering and Industrial Aerodynamics 155 (2016) 74-88.
[14] G. Carrilho da Graça, N.C. Daish, P.F. Linden, A two-zone model for natural cross-ventilation, Building and Environment 89 (2015) 72-85.
[15] T. Kurabuchi, M. Ohba, T. Goto, Y. Akamine, T. Endo, M. Kamata, Local Dynamic Similarity Concept as Applied to Evaluation of Discharge Coefficients of Cross-Ventilated Buildings-Part 1 Basic Idea and Underlying Wind Tunnel Tests; Part 2 Applicability of Local Dynamic Similarity Concept; Part 3 Simplified Method for Estimating Dynamic Pressure Tangential to Openings of Cross-Ventilated Buildings, International Journal of Ventilation 4(3) (2005) 285.
[16] M. Ohba, T. Kurabuchi, E. Tomoyuki, Y. Akamine, M. Kamata, A. Kurahashi, Local Dynamic Similarity Model of Cross-Ventilation Part 2-Application of Local Dynamic Similarity Model, International Journal of Ventilation 2(4) (2004) 383-394.
[17] C.-R. Chu, B.-F. Chiang, Wind-driven cross ventilation in long buildings, Building and Environment 80 (2014) 150-158.
[18] I. Lee, S. Lee, G. Kim, J. Sung, S. Sung, Y. Yoon, PIV verification of greenhouse ventilation air flows to evaluate CFD accuracy, TRANSACTIONS-AMERICAN SOCIETY OF AGRICULTURAL ENGINEERS 48(6) (2005) 2277.

[19] T. Norton, J. Grant, R. Fallon, D.-W. Sun, Improving the representation of thermal boundary conditions of livestock during CFD modelling of the indoor environment, Computers and Electronics in Agriculture 73(1) (2010) 17-36.
[20] M. Teitel, G. Ziskind, O. Liran, V. Dubovsky, R. Letan, Effect of wind direction on greenhouse ventilation rate, airflow patterns and temperature distributions, Biosystems Engineering 101(3) (2008) 351-369.
[21] T. van Hooff, B. Blocken, Y. Tominaga, On the accuracy of CFD simulations of cross-ventilation flows for a generic isolated building: comparison of RANS, LES and experiments, Building and Environment (2016).
[22] Y.-H. Chiu, D. Etheridge, Experimental technique to determine unsteady flow in natural ventilation stacks at model scale, Journal of wind engineering and industrial aerodynamics 92(3) (2004) 291-313.
[23] L. Ji, H. Tan, S. Kato, Z. Bu, T. Takahashi, Wind tunnel investigation on influence of fluctuating wind direction on cross natural ventilation, Building and Environment 46(12) (2011) 2490-2499.
[24] Y. Jiang, D. Alexander, H. Jenkins, R. Arthur, Q. Chen, Natural ventilation in buildings: measurement in a wind tunnel and numerical simulation with large-eddy simulation, Journal of Wind Engineering and Industrial Aerodynamics 91(3) (2003) 331-353.
[25] L.J. Lo, A. Novoselac, Cross ventilation with small openings: Measurements in a multi-zone test building, Building and Environment 57 (2012) 377-386.
[26] J.S. Park, Long-term field measurement on effects of wind speed and directional fluctuation on wind-driven cross ventilation in a mock-up building, Building and Environment 62 (2013) 1-8.
[27] M.H. Sherman, I.S. Walker, M.M. Lunden, Uncertainties in air exchange using continuous-injection, long-term sampling tracer-gas methods, International Journal of Ventilation 13(1) (2014) 13-28.
[28] S. Kato, Flow network model based on power balance as applied to cross-ventilation, International journal of ventilation 2(4) (2004) 395-408.
[29] G.N. Walton, AIRNET: a computer program for building airflow network modeling, National Institute of Standards and Technology Gaithersburg, MD, USA1989.
[30] U. DoE, Energyplus engineering reference, The reference to energyplus calculations (2010).
[31] P. Karava, T. Stathopoulos, A.K. Athienitis, Wind-induced natural ventilation analysis, Solar Energy 81(1) (2007) 20-30.
[32] S. Kato, S. Murakami, A. Mochida, S.-i. Akabayashi, Y. Tominaga, Velocity-pressure field of cross ventilation with open windows analyzed by wind tunnel and numerical simulation, Journal of Wind Engineering and Industrial Aerodynamics 44(1-3) (1992) 2575-2586.
[33] H. Breesch, A. Janssens, Performance evaluation of passive cooling in office buildings based on uncertainty and sensitivity analysis, Solar energy 84(8) (2010) 1453-1467.
[34] D. Costola, B. Blocken, J. Hensen, Overview of pressure coefficient data in building energy simulation and airflow network programs, Building and Environment 44(10) (2009) 2027-2036.
[35] D. Cóstola, B. Blocken, J. Hensen, Uncertainties due to the use of surface averaged wind pressure coefficients, Proceedings of the 29th AIVC Conference, Kyoto, Japan, 2008, pp. 14-16.
[36] J. Lim, Y. Akashi, R. Ooka, H. Kikumoto, Y. Choi, A probabilistic approach to the energy-saving potential of natural ventilation: Effect of approximation method for approaching wind velocity, Building and Environment 122 (2017) 94-104.
[37] J. Lim, R. Ooka, H. Kikumoto, Effect of diurnal variation in wind velocity profiles on ventilation performance estimates, Energy and Buildings 130 (2016) 397-407.
[38] F. Monari, P. Strachan, Characterization of an airflow network model by sensitivity analysis: parameter screening, fixing, prioritizing and mapping, Journal of Building Performance Simulation 10(1) (2017) 17-36.
[39] P. Karava, T. Stathopoulos, A. Athienitis, Wind driven flow through openings–a review of discharge coefficients, International journal of ventilation 3(3) (2004) 255-266.

[40] S. Murakami, Wind tunnel test on velocity-pressure field of cross-ventilation with open windows, ASHRAE transactions 97 (1991) 525-538.
[41] M. Ohba, T. Kurabuchi, Y. Fugo, T. Endo, Local similarity model of cross-ventilation Part 2 Application, The 8th international conference on air distribution in rooms 'ROOMVENT, 2002, pp. 617-620.
[42] C.R. Chu, Y.-H. Chiu, Y.-J. Chen, Y.-W. Wang, C.-P. Chou, Turbulence effects on the discharge coefficient and mean flow rate of wind-driven cross-ventilation, Building and Environment 44(10) (2009) 2064-2072.
[43] T. Sawachi, N. Ken-ichi, N. Kiyota, H. Seto, S. Nishizawa, Y. Ishikawa, Wind pressure and air flow in a full-scale building model under cross ventilation, International Journal of Ventilation 2(4) (2004) 343-357.
[44] A.F. Handbook, American society of heating, refrigerating and air-conditioning engineers, Inc.: Atlanta, GA, USA (2009).
[45] M.W. Liddament, Air infiltration calculation techniques: An applications guide, Air Infiltration and Ventilation Centre Berkshire, UK1986.
[46] M. Grosso, Wind pressure distribution around buildings: a parametrical model, Energy and Buildings 18(2) (1992) 101-131.
[47] B. Knoll, J. Phaff, W. De Gids, Pressure simulation program, Implementing the Results of Ventilation Research, 16th AIVC conference, 19-22 September 1995, Palm Springs, USA, TNO, 1995.
[48] M. Swami, S. Chandra, Correlations for pressure distribution on buildings and calculation of natural-ventilation airflow, ASHRAE transactions 94(3112) (1988) 243-266.
[49] B. Wang, T. Dogan, D. Pal, C. Reinhart, SIMULATING NATURALLY VENTILATED BUILDINGS WITH DETAILED CFD-BASED WIND PRESSURE DATABASE, IBPSA-USA Journal 5(1) (2012) 353-360.
[50] R. Jin, W. Chen, A. Sudjianto, An efficient algorithm for constructing optimal design of computer experiments, Journal of Statistical Planning and Inference 134(1) (2005) 268-287.
[51] Y. Tamura, Aerodynamic database for low-rise buildings, Global Center of Excellence Program, Tokyo Polytechnic University, Database (2012).
[52] M.E. Johnson, L.M. Moore, D. Ylvisaker, Minimax and maximin distance designs, Journal of statistical planning and inference 26(2) (1990) 131-148.
[53] R.H. Myers, D.C. Montgomery, G.G. Vining, C.M. Borror, S.M. Kowalski, Response surface methodology: a retrospective and literature survey, Journal of quality technology 36(1) (2004) 53.
[54] D.S. Broomhead, D. Lowe, Radial basis functions, multi-variable functional interpolation and adaptive networks, DTIC Document, 1988.
[55] E.J. Kansa, Motivation for using radial basis functions to solve PDEs, RN 64(1) (1999) 1.
[56] D. Cóstola, B. Blocken, M. Ohba, J. Hensen, Uncertainty in airflow rate calculations due to the use of surface-averaged pressure coefficients, Energy and Buildings 42(6) (2010) 881-888.
[57] T. Nozu, T. Tamura, Y. Okuda, S. Sanada, LES of the flow and building wall pressures in the center of Tokyo, Journal of Wind Engineering and Industrial Aerodynamics 96(10) (2008) 1762-1773.
[58] T. Yang, N. Wright, D. Etheridge, A. Quinn, A comparison of CFD and full-scale measurements for analysis of natural ventilation, International Journal of Ventilation 4(4) (2006) 337-348.
[59] P. Richards, S. Norris, Appropriate boundary conditions for computational wind engineering models revisited, Journal of Wind Engineering and Industrial Aerodynamics 99(4) (2011) 257-266.
[60] R. Akins, J. Peterka, J. Cermak, Averaged pressure coefficients for rectangular buildings, Wind Engineering 1 (1979) 369,380.
[61] G. Walton, W. Dols, CONTAM 2.1 Supplemental user guide and program documentation. 2006, Gaithersburg, MD: National Institute of Standards and Technology Google Scholar (2006).
[62] R. Aynsley, W. Melbourne, B. Vickery, Architectural aerodynamics, 1977.

[63] C.M. Rhie, W.L. Chow, Numerical study of the turbulent flow past an airfoil with trailing edge separation, AIAA Journal 21(11) (1983) 1525-1532.
[64] A. CFX, Solver Theory Guide. Ansys, Inc., Canonsburg, PA (2011).
[65] Y. Tominaga, A. Mochida, R. Yoshie, H. Kataoka, T. Nozu, M. Yoshikawa, T. Shirasawa, AIJ guidelines for practical applications of CFD to pedestrian wind environment around buildings, Journal of wind engineering and industrial aerodynamics 96(10) (2008) 1749-1761.
[66] P.A. Mirzaei, J. Carmeliet, Dynamical computational fluid dynamics modeling of the stochastic wind for application of urban studies, Building and Environment 70 (2013) 161-170.
[67] J. Franke, Best practice guideline for the CFD simulation of flows in the urban environment, Meteorological Inst.2007.
[68] D.C. Montgomery, Design and analysis of experiments, John Wiley & Sons2017.
[69] B.F. Ryan, B.L. Joiner, Minitab handbook, Duxbury Press2001.